



Hydrogen adsorption-induced catalytic enhancement over Cu nanoparticles immobilized by layered Ti_3C_2 MXene



Lijun Liu^{a,b,*}, Qing Zhao^a, Rong Liu^a, Leifan Zhu^a

^a College of Chemistry and Chemical Engineering, Wuhan Textile University, Wuhan, 430200, China

^b Hubei Key Laboratory of Biomass Fibers and Eco-dyeing & Finishing, Wuhan Textile University, Wuhan, 430200, China

ARTICLE INFO

Keywords:

MXene
Electron transfer
d-Band center
4-Nitrophenol
Hydrogen adsorption energy

ABSTRACT

Electronic interaction at metal/support interfaces could change the electronic structure and catalytic activity of a metal. Herein, Cu nanoparticles (NPs) with sizes of ~5 nm were uniformly deposited on two-dimensional titanium carbide MXene (Ti_3C_2). Some electrons transferred from Cu to Ti_3C_2 upon hybridization as evidenced by XPS analysis and DFT calculations. The work function (5.78 eV) of Ti_3C_2 was higher than that (4.63 eV) of Cu NPs, which was responsible for the interfacial charge transfer. Upon formation of Cu/ Ti_3C_2 , the d-band center (ϵ_d) of Cu was shifted upwards from –2.38 eV to –2.27 eV with reference to Fermi energy. The calculated hydrogen adsorption energy (–2.57 eV) of Cu/ Ti_3C_2 was higher than that (–2.45 eV) of unsupported Cu NPs. Such favorable hydrogen adsorption of Cu/ Ti_3C_2 increased the number of surface-adsorbed hydrogen atoms, beneficial for the hydrogen-involved redox from the viewpoint of kinetics. Cu/ Ti_3C_2 showed a promising catalytic activity for the reduction of 4-nitrophenol into 4-aminophenol with a normalized rate constant of $43.1 \text{ min}^{-1} \text{ mg}^{-1}$, which was 6.3 times as high as that of Cu NPs. Such enhanced catalysis was ascribed to the favorable hydrogen adsorption and good hydrophilicity of the nanohybrid. This work presents an example that the catalytic activity of Ti_3C_2 MXene-supported metals can be promoted by their hydrogen adsorption, which will broaden the application of other 2D MXene materials in catalysis.

1. Introduction

Converting toxic 4-nitrophenol (4-NP) to useful 4-aminophenol (4-AP) is desired for environmental protection and sustainable development [1–3]. 4-NP can be reduced to 4-AP by sodium borohydride over metal nanocatalysts, where active hydrogen atoms produced from the B–H cleavage are the actual reductant for 4-NP reduction [4–13]. Noble metal Pd is one of the most efficient catalysts for the redox owing to its favourable chemisorption of active hydrogen atoms to form Pd–H species, which kinetically promotes the surface redox [14–19]. Despite Pd reveals high efficiency for the reaction, its scarcity and cost limit the practical application, pushing forwards an intensive exploration of cost-effective alternative catalysts.

Cu is a cheap and earth-abundant transition metal and was found to be catalytically active for the redox [20–28]. Generally, the reduction of 4-NP by active hydrogen atoms follows a Langmuir–Hinshelwood kinetic model, where both hydrogen atoms and 4-NP molecules should be adsorbed onto metals prior to surface reaction [29,30]. Thus, apart from the intrinsic catalytic activity of metals, appropriate hydrogen adsorption also exerts much importance on the kinetics of 4-NP

reduction [31,32]. Unlike the favourable hydrogen affinity of Pd (Pd–H bond), Cu shows less adsorption of hydrogen atoms due to its unique electronic structure [33]. Density functional theory (DFT) simulation unfolded that the hydrogen adsorption energy over Cu is –2.45 eV, which is smaller than that (–2.88 eV) of Pd [34]. Inspired by this, we speculate that promoting the adsorption of active hydrogen atoms onto Cu surface could be an effective strategy to promote the 4-NP reduction.

According to the d-band model proposed by Nørskov, hydrogen adsorption over a transition metal largely correlates with its d-electrons [35]. The d-band of a transition metal with adsorbate is composed of empty antibonding states above Fermi level and filled bonding states below Fermi level [36,37]. The fraction of antibonding states is related with the d-band center (ϵ_d) of the metal, thus ϵ_d becomes an important descriptor to describe the adsorption capability of a transition metal [38]. It is accepted that immobilizing metal nanoparticles (NPs) on a support could change their electronic structure (ϵ_d) and the hydrogen adsorption behavior [39], which eventually influences the catalytic activity owing to the strong metal/support interaction (SMSI) effect [40–42].

Titanium carbide MXene (Ti_3C_2) is an emerging layered material,

* Corresponding author at: 1 Yangguang Avenue, Jiangxia District, Wuhan, 430200, China.

E-mail address: liulj@wtu.edu.cn (L. Liu).

which has motivated much interest in the community of catalysis, electronics, and energy storage [43–47]. Ti_3C_2 could be a support for hosting Cu NPs due to its conductivity, hydrophilicity and large specific surface area [48]. Moreover, electrons within the layered Ti_3C_2 are prone to delocalization, which could enable an electron transfer at the $\text{Cu}/\text{Ti}_3\text{C}_2$ interfaces upon their hybridization [49]. Such an electron transfer should change the intrinsic electronic states and influence the kinetics of 4-NP reduction over Cu NPs [50].

Herein, Cu NPs were hybridized with two-dimensional (2D) layered Ti_3C_2 MXene via a solution-phase synthesis to promote the catalytic reduction of 4-NP. The electronic structure of Cu NPs was slightly changed after hybridization with Ti_3C_2 due to the presence of interfacial electron transfer from Cu to Ti_3C_2 as evidenced by XPS and DFT results. The upshifted d-band center of Cu and favorable hydrogen adsorption were responsible for the promising catalysis of $\text{Cu}/\text{Ti}_3\text{C}_2$. This is the first example to explore the effect of hydrogen adsorption on catalysis over Cu metals for the 4-NP reduction, which could provide new insights into the design of other advanced catalysts for hydrogen transfer reaction.

2. Results and discussion

2.1. Phase and morphology

The $\text{Cu}/\text{Ti}_3\text{C}_2$ nanohybrid was synthesized by depositing Cu NPs onto layered Ti_3C_2 MXene through a solution-phase reduction method [51]. The experimental and computational details can be found in the *Supplementary material*. For convenience, the resulting $\text{Cu}/\text{Ti}_3\text{C}_2$ is labeled as CT_x , where C and T represent Cu and Ti_3C_2 MXene respectively; and x is the nominal weight percentage of Cu loading in the hybrid. The actual loading of Cu NPs in each CT_x was measured by ICP-OES and presented in Table S1.

Fig. 1 shows the XRD patterns of pristine Ti_3C_2 and CT_x nanohybrids. Each pattern exhibits a series of characteristic $(00l)$ reflections, revealing a layered structures of Ti_3C_2 Mxene. The interplanar distance estimated from (002) reflection is 1.29 nm [52]. The appearance of the reflection at $2\theta = 27.5^\circ$ is related to the insertion of OH groups [47]. Upon hybridization with Cu NPs, there appear additional weak reflections matching well with crystalline Cu with fcc structure (JCPDS # 04-0836). The intensity of Cu reflections is enhanced as the Cu loading is increased. Aside from the intensity change, the (002) reflection of Ti_3C_2 shows an apparent shift towards a lower 2θ value. The (002) d -spacing

of Ti_3C_2 in CT_{12} is estimated to be 1.51 nm, significantly larger than that of pristine Ti_3C_2 , which could be ascribed to the intercalation of Na^+ ions or Cu nanoclusters into Ti_3C_2 layers during the reaction process.

As shown in the SEM image of Fig. 2a, pristine Ti_3C_2 reveals a layered accordion-like microstructure with smooth surfaces after the chemical etching of its Ti_3AlC_2 precursor. After coupled with Cu NPs, Ti_3C_2 still reserves the layered structure but is covered by a great number of Cu NPs (Fig. 2b), implying good structural stability of Ti_3C_2 and successful formation of $\text{Cu}/\text{Ti}_3\text{C}_2$ nanohybrids. Such Cu NPs are uniformly distributed onto Ti_3C_2 nanosheets and have diameters of ~5 nm estimated from the enlarged SEM image of Fig. 2c. It is generally believed that Ti_3C_2 MXene is unstable and ready for oxidation in oxygen-containing aqueous solution [53]. In this work, however, Ti_3C_2 maintains its original phase and morphology during the synthesis possibly because of the low reaction temperature (0°C) and the H_2 atmosphere generated from the NaBH_4 decomposition. Fig. 2d shows the EDX spectrum of CT_{12} , revealing the presence of Cu, C, Ti, F, O and Na elements. The O and F elements originate from the surface terminations of Ti_3C_2 . The presence of Na signal implies that Na^+ ions were incorporated into Ti_3C_2 interlayers during the NaBH_4 -involved solution-phase synthesis. The exact loading of Cu NPs is determined to be 12.2 wt.% by ICP-OES, which is comparable with its nominal loading (12 wt.%) estimated from the feeding precursors.

The morphology and crystalline phase were further explored with use of TEM and HRTEM. The TEM image (Fig. 3a) reveals that CT_{12} is composed of stacked Ti_3C_2 flakes as well as Cu NPs (~5 nm) closely depositing on the flakes, consistent with above SEM observation. It is found Cu NPs in CT4 and CT8 have a similar size of ~5 nm and show no apparent aggregation, while Cu NPs in CT16 and CT20 show slight aggregation due to the overloading (Fig. S1). The HRTEM image (Fig. 3b) of CT_{12} shows clear lattice fringes with an interplanar spacing of 1.51 nm from Ti_3C_2 (002) facets. The deposited Cu nanoparticle (inset of Fig. 3b) exhibits lattice fringes with a d -spacing of 0.209 nm, corresponding to the (111) facets of fcc Cu. The result matches well with the XRD analysis and confirms the successful preparation of $\text{Cu}/\text{Ti}_3\text{C}_2$ nanohybrid.

N_2 sorption isotherms were recorded to explore the specific surface areas (S_{BET}) and pores of Ti_3C_2 and CT_x (Fig. 4 and Fig. S2). Each sample shows a IV-type isotherm with an apparent H3-type hysteresis loop in the P/P_0 range of 0.6~1.0 according to the IUPAC classification, indicating the existence of slit-like pores that might derive from the inter-nanosheet spacing of accordion-like Ti_3C_2 [54]. The pore size distribution of each sample is estimated from the adsorption branch of the isotherms (inset of Fig. 4), which shows a broad pore distribution centered at ~70 nm due to the particle stacking of Ti_3C_2 particles. Apart from the mesopores (~70 nm), CT_{12} has an apparent nanopores (<3 nm) from the deposition of Cu NPs into and/or onto layered Ti_3C_2 MXene. CT_{12} shows a much higher S_{BET} of $23.8 \text{ m}^2 \text{ g}^{-1}$ than pristine Ti_3C_2 ($4.0 \text{ m}^2 \text{ g}^{-1}$) owing to the presence of nanopores and the rough surface of Ti_3C_2 layers upon hybridization.

2.2. Chemical states

The chemical state and surface composition of CT_{12} were characterized by X-ray photoelectron spectroscopy (XPS). The C 1 s XPS spectrum of CT_{12} (Fig. 5a) reveals the presence of four kinds of carbon species. The intensive signal at 284.6 eV is originated from C-C within Ti_3C_2 or carbon impurities from the testing tape. The others correspond to C-Ti, C=O, C=O and/or C-F, respectively. The Ti 2p XPS spectrum (Fig. 5b) of CT_{12} shows two dominant signals belonging to $\text{Ti} 2p_{1/2}$ (454.9 eV) and $2p_{3/2}$ (461.0 eV) of Ti-C. The weak signals at 458.5 and 464.3 eV are identified as $\text{Ti} 2p$ doublets of Ti-O from the oxygen-containing termination on the surface of Ti_3C_2 MXene [55,56]. The O 2p XPS spectrum (Fig. 5c) unfolds two kinds of O species of surface $\text{Ti}-\text{OH}$ (531.2 eV) and adsorbed H_2O (532.9 eV) [57]. Fig. 5d shows

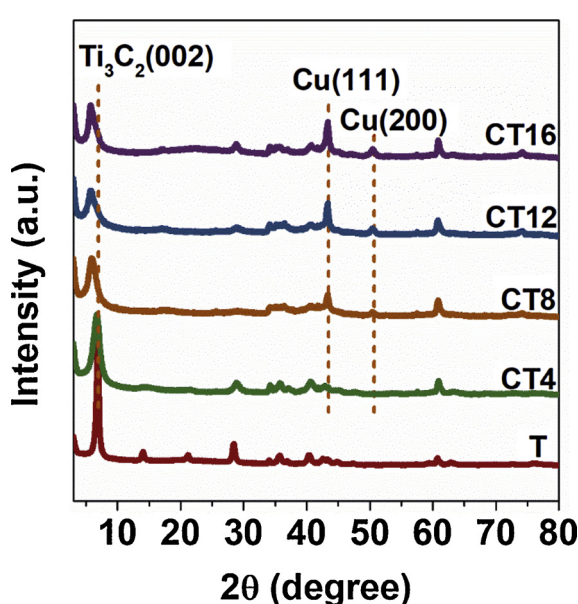


Fig. 1. XRD patterns of pristine Ti_3C_2 and CT_x with various loadings of Cu NPs.

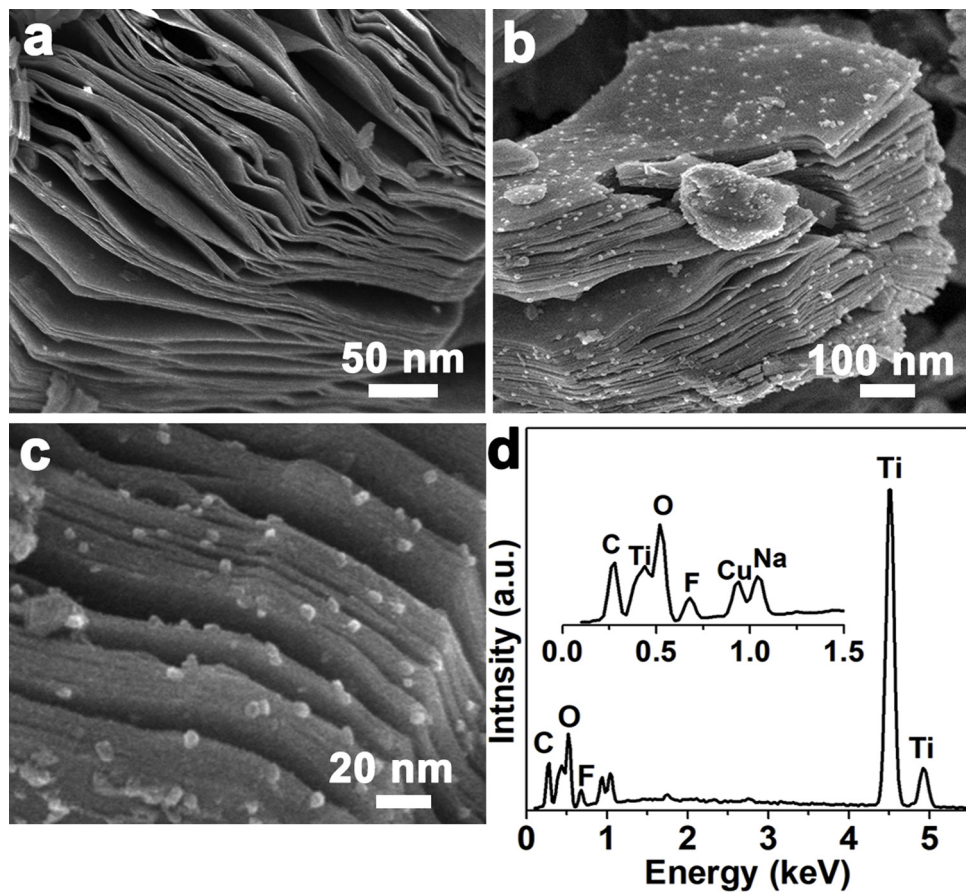


Fig. 2. SEM images of (a) pristine Ti_3C_2 and (b–c) CT12 nanohybrid. (c) EDX spectrum of the CT12 nanohybrid.

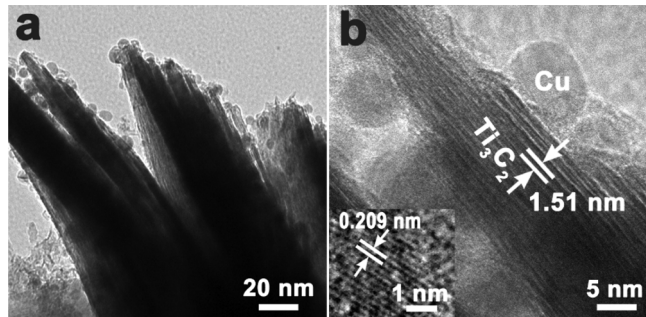


Fig. 3. (a) TEM and (b) HRTEM images of the CT12 nanohybrid. Inset: HRTEM image of a single Cu nanoparticle in CT12.

the Cu 2p XPS spectra of Cu and CT12, both of which unfold the presence of zerovalent Cu in each sample [58]. Noted that the binding energy (BE) of Cu 3p_{3/2} of CT12 is slightly larger (+ 0.3 eV) than that of Cu NPs, suggesting the presence of electron transfer from Cu to Ti_3C_2 upon their contact [59–61]. Such a BE shift is also found in the XPS spectra of CT4, CT8, CT16 and CT20 (Fig. S3), implying the electron transfer is independent of the loading amount of Cu NPs.

2.3. Interfacial electron transfer

The charge transfer at Cu/ Ti_3C_2 interfaces was further explored by using DFT calculations. Work function (ϕ) is well-accepted indication to predict charge transfer at interfaces of a hybrid. It is defined as the minimum energy needed to extract an electron from a solid surface into vacuum. A phase with lower ϕ will donate electrons to that with higher ϕ when two phase combine to form a nanohybrid [62]. Fig. 6 shows the

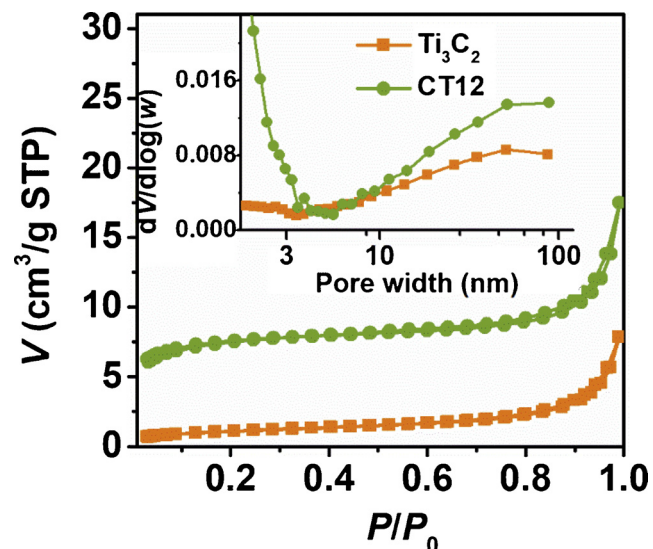


Fig. 4. N_2 sorption isotherms and pore size distributions (inset) of the pristine Ti_3C_2 and CT12.

electrostatic potentials along c axis of Cu (111) and Ti_3C_2 (001) slabs. The ϕ values of Cu (111) and Ti_3C_2 (001) slabs are calculated to be 4.63 eV and 5.78 eV in terms of their Fermi and vacuum energy levels, which are comparable with the work functions measured by using ultraviolet photoelectron spectroscopy (UPS) as shown in Fig. S4. Clearly, Cu shows much lower ϕ than that of Ti_3C_2 , suggesting that some electrons of Cu will transfer into Ti_3C_2 upon their combination.

Charge density calculations were also performed to explore the

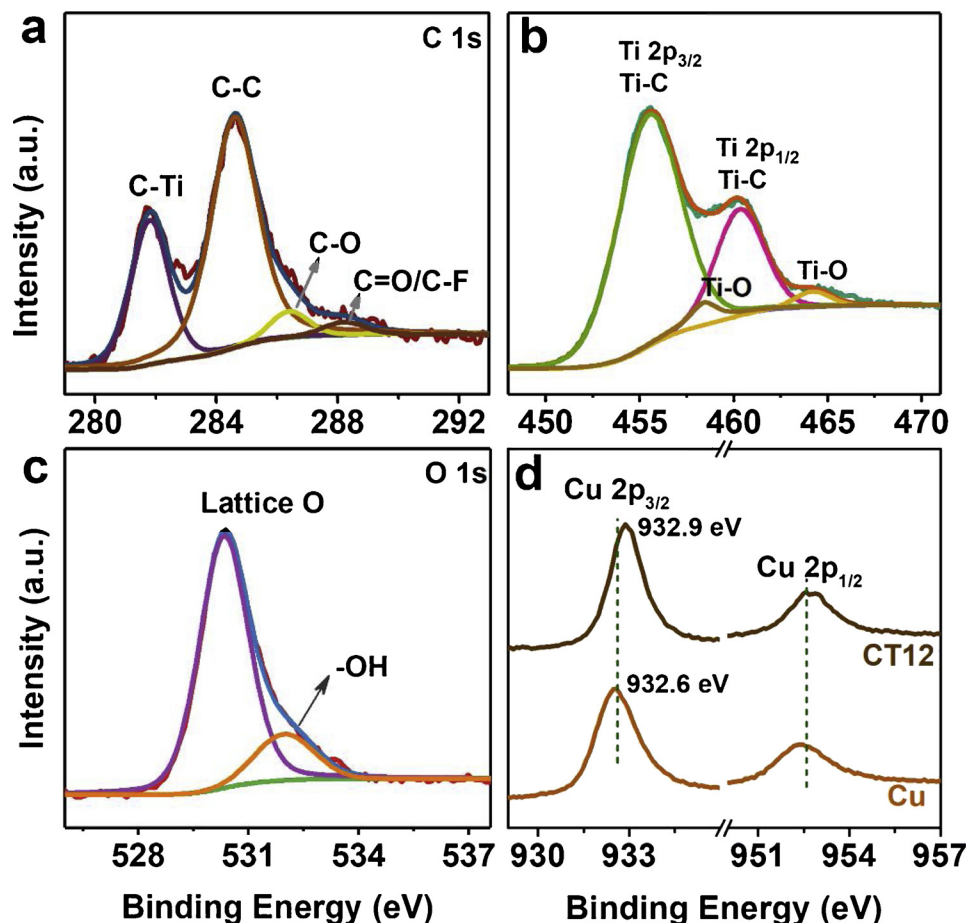


Fig. 5. XPS spectra of (a) C 1 s, (b) Ti 2p and (c) O 1s of CT12. (d) Cu 2p core level XPS spectra of Cu NPs and CT12.

electronic coupling between Cu and Ti_3C_2 . Fig. 7a shows the line profile of plane-averaged differential charge density ($\Delta\rho$) along z direction of the model. There appears an intensive $\Delta\rho$ oscillation at the Cu/ Ti_3C_2 interface, suggesting a remarkable redistribution of surface charge [63]. The differential charge density shown in Fig. 7b provides information about the electron redistribution between Cu and Ti_3C_2 . Clearly, the bottom Cu atoms of Cu (111) slab donate electrons to the interfacial O atoms of Ti_3C_2 (002) slab. Bader charge analysis shows that the electrons donated from Cu to Ti_3C_2 amount to 1.54 e (equivalent to 0.0644 e per Cu atom). The findings reaffirm the occurrence of the Cu-to- Ti_3C_2 electron transfer upon hybridization. Such electron transfer changes the electronic structure of Cu NPs and eventually promotes their catalytic

activity as discussed below.

2.4. Catalytic performance

4-NP cannot be reduced by NaBH_4 without a catalysts despite the thermodynamic feasibility [4]. In the presence of CT12, 4-NP was rapidly reduced as evidenced by a decrease of 4-NP (400 nm) along with an increase of 4-AP (302 nm) (Fig. 8a). Only two isosbestic points are present in the wavelength range, implying no by-product was formed during the reaction [64]. Pristine Ti_3C_2 and CT12 are hydrophilic (Fig. S5) and readily dispersed in aqueous solution. Fig. 8b reveals the kinetic plots of the redox over Cu, Ti_3C_2 and CT12. Pristine Ti_3C_2 shows

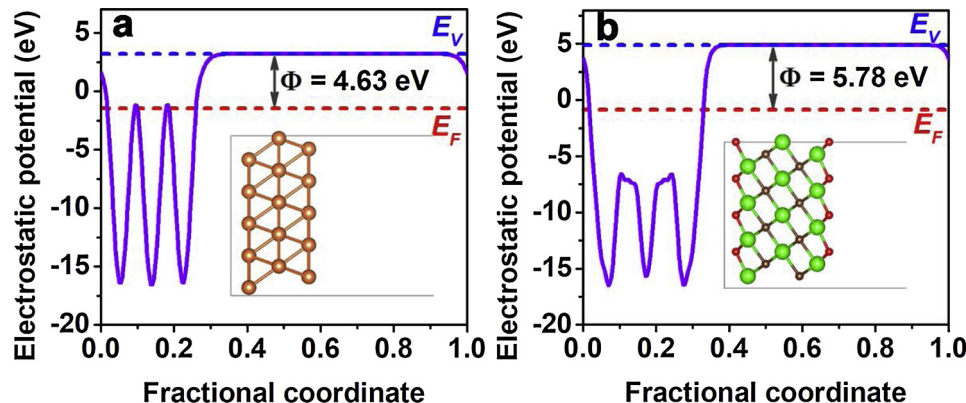


Fig. 6. The electrostatic potentials along c axis of (a) Cu (111) and (b) Ti_3C_2 (001) slabs. The red and blue dashed lines denote the Fermi and vacuum energy levels, respectively (For interpretation of the references to colour in this figure legend, the reader is referred to the web version of this article).

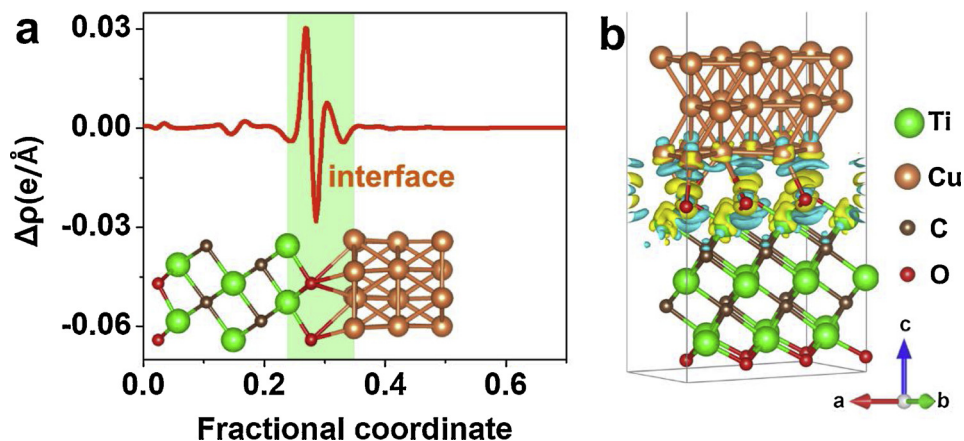


Fig. 7. (a) Profile of the plane-averaged differential charge density along z-axis of Cu/Ti₃C₂ model shown in the inset. (b) the corresponding isosurface of differential charge density. Cyan and yellow colors denote electron depletion and accumulation, respectively (For interpretation of the references to colour in this figure legend, the reader is referred to the web version of this article).

no catalytic activity, implying that Cu is the active component for the redox. The linear $\ln(C_t/C_0)$ ~t plots reveal the redox follows pseudo-first-order kinetics because of the excessive NaBH₄. The apparent rate constant (k) of CT12 from the linear correlation is calculated to be 0.673 min^{-1} , which is 6.3 times as high as that of free Cu NPs (0.107 min^{-1}).

The mass loading of Cu (x) influences the apparent k and normalized k_n ($k_n = k / m_{\text{Cu}}$) of CT_x as shown in Fig. 8c. As x increases from 0 to 0.12, the apparent k of the redox is linearly increased with a constant k_n of $\sim 43.1 \text{ min}^{-1} \text{ mg}^{-1}$, implying the catalytic redox is a surface-mediated reaction. In fact, the chemisorbed hydrogen atoms on Cu NPs are the actual reductant [4]. CT_x with a higher Cu loading offers more active sites for hydrogen adsorption and thus exhibits a more favorable

kinetics. Further increasing x up to 0.2 (CT20) leads to a low k_n of $33.8 \text{ min}^{-1} \text{ mg}^{-1}$, showing that per unit mass of Cu contributes less activity than that of CT12 owing to the overloading of Cu NPs.

We also evaluated the catalytic activity of Cu/Ti₃C₂ for the reduction of 4-nitrotoluene and 4-nitrochlorobenzene. It is found the TOF (0.026 min^{-1}) of 4-nitrotoluene reduction over CT12 is higher than that (0.016 min^{-1}) of 4-nitrochlorobenzene reduction (Table S2), indicating an electron-releasing substituent ($-CH_3$) is favorable for the reduction of nitrobenzenes into amines over the catalyst. The Cu NPs in CT4, CT8 and CT12 have similar sizes of $\sim 5 \text{ nm}$ (Fig. S1) and a similar TOF for the 4-NP reduction (Table S1), showing no apparent size effect on the catalysis. The TOF decrease of CT16 and CT20 is ascribed to the aggregation of Cu NPs that reduces the number of catalytically active

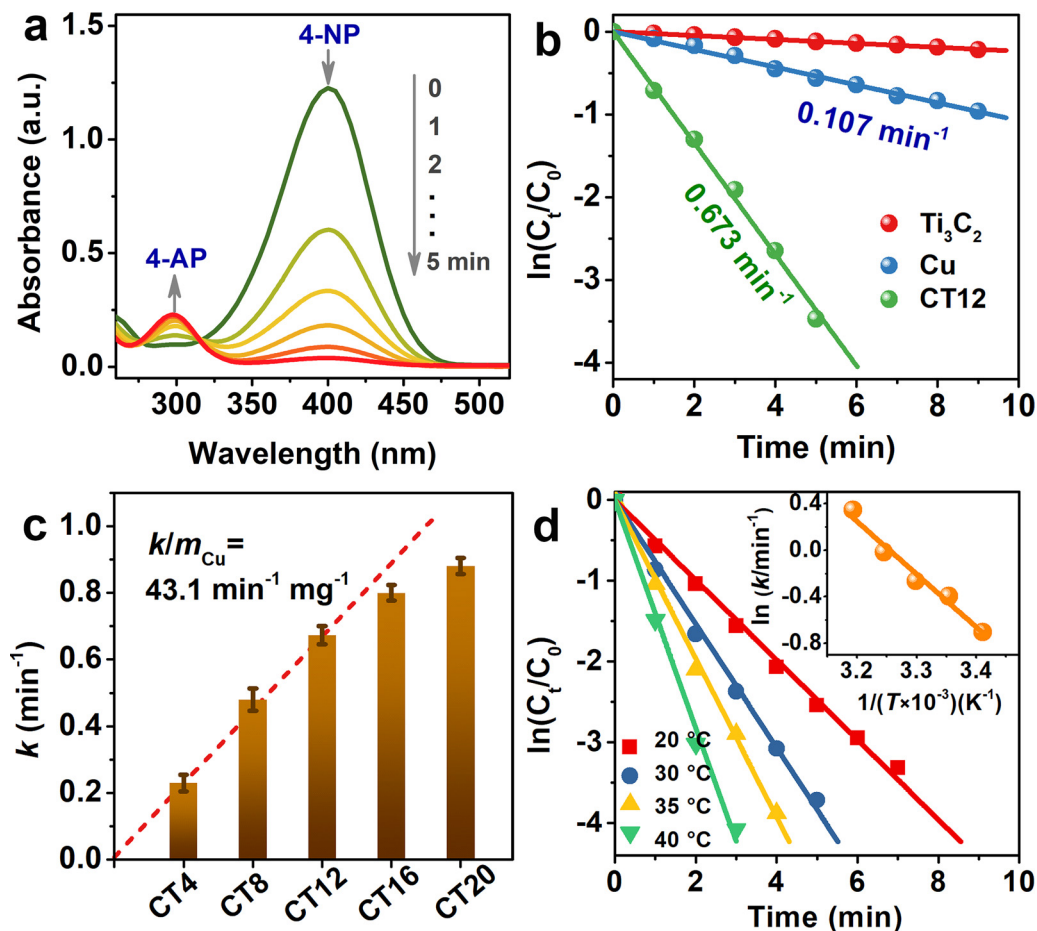


Fig. 8. (a) Time-course UV-vis absorption spectra for the reduction of 4-NP over CT12. (b) Kinetic plots of the redox over Cu, Ti₃C₂ and CT12 samples at 25 °C. (c) Apparent rate constant of the redox over Cu/Ti₃C₂ with various Cu loadings at 25 °C. (d) Kinetic plots of the redox over CT12 at different reaction temperatures and the corresponding Arrhenius plot (inset).

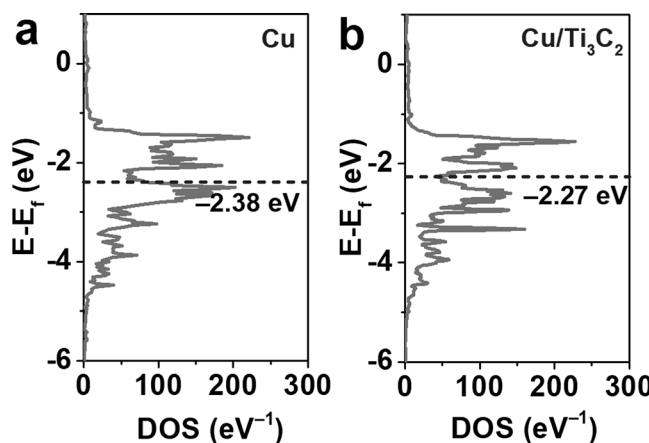


Fig. 9. Projected density of states (DOS) onto Cu 3d orbitals of (a) Cu and (b) Cu/Ti₃C₂ models. The d-band center ϵ_d is indicated by dash line.

sites.

Table S3 compares the catalytic activity of CT12 with previous catalysts in terms of the turnover frequency (TOF). Clearly, CT12 (1.025 min^{-1}) is superior to previous Cu catalysts, e.g., Cu cages (0.133 min^{-1}) [27], Cu hollow NPs (0.049 min^{-1}) [26], and is comparable with some Pd catalyst, e.g., Pd/N-doped graphene (0.998 min^{-1}) [50].

The activation energy (E_a) estimated from the $\ln k^{\circ}/T$ plot is as low as $36.1 \text{ kJ}\cdot\text{mol}^{-1}$ (Fig. 8d), revealing a low kinetic barrier for 4-NP reduction in the presence of CT12. The recyclability of samples was also examined. After five cycling usages, CT12 maintains 95.4% of catalytic activity (Fig. S6). The spent CT12 contains 11.8 wt% of Cu from ICP-OES analysis, a little lower than its initial value (12.2 wt%). The phase of the spent CT12 is unchanged (Fig. S7) and all the diffraction peaks correspond to either Cu or Ti₃C₂. The TEM images of the spent CT12 (Fig. S8a-b) show the presence of particle aggregation after cycling uses. The Ti 2p XPS spectrum (Fig. S8c) of the spent CT12 agree with that of pristine Ti₃C₂. The Cu 2p XPS spectrum (Fig. S8d) reveals the presence of zerovalent Cu in the sample. Thus, the slight activity loss could be ascribed to the detachment of Cu NPs from Ti₃C₂ and the particle aggregation during cycling usage.

2.5. Catalytic mechanism

The reduction of 4-NP by NaBH₄ is a model reaction, where active hydrogen atoms from B–H breakage is the exact reductant for the redox [4]. It is established that the 4-NP reduction follows a Langmuir–Hinshelwood kinetic model [65,66]. This means that both active hydrogen atoms and 4-NP should be adsorbed onto metals prior to surface reaction. Thus, effective adsorption of active hydrogen atoms over Cu NPs is kinetically favourable for the 4-NP reduction.

On the basis of d-band model suggested by Nørskov et al., the hydrogen adsorption of a transition metal correlates with its d-band center (ϵ_d) [35]. Metal with a higher ϵ_d often exhibits a favorable hydrogen affinity owing to the presence of more unfilled antibonding states within the d-band [31]. As unfolded by above XPS analysis and DFT calculations, there exists electron transfer from Cu to Ti₃C₂ upon hybridization. Such electron transfer could change the electronic state and d-band center (ϵ_d) of Cu. Fig. 9 shows the projected density of states (DOS) on Cu 3d orbitals for Cu and Cu/Ti₃C₂. The ϵ_d of Cu atoms in Cu/Ti₃C₂ is -2.27 eV , which is higher than that (-2.38 eV) of pristine Cu. The higher ϵ_d means that Ti₃C₂-supported Cu NPs can provide more empty antibonding d-bands for active hydrogen atoms and thus exhibit stronger adsorption to active hydrogen atoms [67].

Bearing these in mind, we have compared the hydrogen adsorption energy (E_{ad}) of Cu and Cu/Ti₃C₂ by means of DFT calculations. After

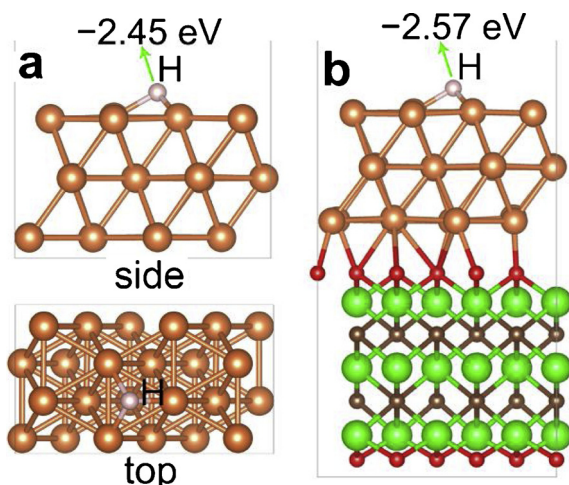


Fig. 10. Optimized adsorption configuration of H atom over the hcp hollow site of (a) Cu(111) and (b) Cu(111)/Ti₃C₂(001) surface slabs.

screening four kinds of possible adsorption sites (fcc hollow, hcp hollow, top, and bridge sites), we found the hcp hollow site on Cu (111) slabs was the most energetically favorable for hydrogen adsorption (Fig. 10). The hydrogen adsorption energy (E_{ad}) is defined as $E_{ad} = E_{\text{slab-H}} - E_{\text{slab}} - E_H$, where $E_{\text{slab-H}}$, E_{slab} and E_H are the energy of surface slab after hydrogen adsorption, surface slab and single H atom, respectively. As expected, Cu/Ti₃C₂ (-2.57 eV) shows a higher E_{ad} than pristine Cu (-2.45 eV). The enhanced hydrogen adsorption over Cu/Ti₃C₂ facilitates the 4-NP reduction, since the redox requires both 4-NP and active hydrogen atoms to be adsorbed on metals prior to surface reaction. As a result, it is concluded that the superior activity of Cu/Ti₃C₂ is derived from the favorable hydrogen adsorption of Cu NPs as well as the large S_{BET} and good hydrophilicity of Ti₃C₂ MXene.

3. Conclusions

Cu NPs (~5 nm) were immobilized onto layered Ti₃C₂ MXene via a low-temperature solution-phase synthesis. DFT calculation and XPS result prove that some electrons immigrate from Cu to Ti₃C₂ upon combination. The charge transfer alters the density of state and upshifts its d-band center of Cu NPs, which leads to an enhanced adsorption of active hydrogen atoms. The calculated hydrogen adsorption energy for Cu NPs increased from -2.57 eV to -2.45 eV after hybridization with Ti₃C₂ MXene. Such a favorable adsorption increases the number of active hydrogen atoms on Cu NPs, kinetically beneficial to the 4-NP reduction. The resulting Cu/Ti₃C₂ shows an enhanced catalytic activity for the reduction of 4-NP to 4-AP with a high k_n ($43.1 \text{ min}^{-1} \text{ mg}^{-1}$), 6.3 times as high as that of Cu NPs. The superior catalytic activity of Cu/Ti₃C₂ can be ascribed to the favorable adsorption of active hydrogen atoms and good hydrophilicity of Ti₃C₂ MXene.

Acknowledgements

This work was supported by the National Natural Science Foundation of China (No. 51201116 and No. 51310105015).

Appendix A. Supplementary data

Supplementary material related to this article can be found, in the online version, at doi:<https://doi.org/10.1016/j.apcatb.2019.04.026>.

References

- [1] T. Aditya, A. Pal, T. Pal, Chem. Commun. (Camb.) 51 (2015) 9410–9431.
- [2] Z. Yan, L. Fu, X. Zuo, H. Yang, Appl. Catal. B 226 (2018) 23–30.

[3] X. Pan, X. Gao, X. Chen, H.N. Lee, Y. Liu, R.L. Withers, Z. Yi, *ACS Catal.* 7 (2017) 6991–6998.

[4] P. Herves, M. Perez-Lorenzo, L.M. Liz-Marzan, J. Dzubiella, Y. Lu, M. Ballauff, *Chem. Soc. Rev.* 41 (2012) 5577–5587.

[5] J.W. Xia, G.Y. He, L.L. Zhang, X.Q. Sun, X. Wang, *Appl. Catal. B* 180 (2016) 408–415.

[6] T.A. Revathy, S. Dhanavel, T. Sivarajanji, V. Narayanan, T. Maiyalagan, A. Stephen, *Appl. Surf. Sci.* 449 (2018) 764–771.

[7] P. İlgin, O. Ozay, *Appl. Catal. B* 241 (2018) 415–423.

[8] E. Numerov, R.A. Hughes, S.D. Golze, R.D. Neal, T.B. Demille, J.C. Campanaro, K.C. Kotesky, S. Rouvimov, S. Neretina, *ACS Catal.* 8 (2018) 8879–8888.

[9] Y. Long, Y. Huang, X. Shi, L. Xiao, J. Mater. Chem. A Mater. Energy Sustain. 6 (2018) 18561–18570.

[10] X.-Q. Wu, J. Zhao, Y.-P. Wu, W.-w. Dong, D.-S. Li, J.-R. Li, Q. Zhang, *ACS Appl. Mater. Interfaces* 10 (2018) 12740–12749.

[11] H. Ma, H. Wang, T. Wu, C. Na, *Appl. Catal. B* 180 (2016) 471–479.

[12] Q. Zhang, X. Jin, Z. Xu, J. Zhang, U.F. Rendon, L. Razzari, M. Chaker, D. Ma, *J. Phys. Chem. Lett.* 9 (2018) 5317–5326.

[13] J. Xi, J. Xiao, F. Xiao, Y. Jin, Y. Dong, F. Jing, S. Wang, *Sci. Rep.* 6 (2016) 21904.

[14] Z. Zhao, X. Huang, M. Li, G. Wang, C. Lee, E. Zhu, X. Duan, Y. Huang, *J. Am. Chem. Soc.* 137 (2015) 15672–15675.

[15] S.K. Movahed, N.F. Lehi, M. Dabiri, *J. Catal.* 364 (2018) 69–79.

[16] J. Liu, J. Hao, C. Hu, B. He, J. Xi, J. Xiao, S. Wang, Z. Bai, *J. Phys. Chem. C* 122 (2018) 2696–2703.

[17] M.G. Sandoval, R. Luna, G. Brizuela, A.O. Pereira, C.R. Miranda, P. Jasen, *J. Phys. Chem. C* 121 (2017) 8613–8622.

[18] J. Xi, H. Sung, D. Wang, Z. Zhang, X. Duan, J. Xiao, F. Xiao, L. Liu, S. Wang, *Appl. Catal. B* 225 (2018) 291–297.

[19] X. Duan, M. Xiao, S. Liang, Z. Zhang, Y. Zeng, J. Xi, S. Wang, *Carbon* 119 (2017) 326–331.

[20] F. Fu, R. Ciganda, Q. Wang, A. Tabey, C. Wang, A. Escobar, A.M. Martinez-Villacorta, R. Hernandez, S. Moya, E. Fouquet, J. Ruiz, D. Astruc, *ACS Catal.* 8 (2018) 8100–8106.

[21] R. Kaur, C. Giordano, M. Gradzielski, S.K. Mehta, *Chem. Asian J.* 9 (2014) 189–198.

[22] C. Wang, R. Ciganda, L. Salmon, D. Gregurec, J. Irigoyen, S. Moya, J. Ruiz, D. Astruc, *Angew. Chem., Int. Ed.* 55 (2016) 3091–3095.

[23] Y. Zhong, Y. Gu, L. Yu, G. Cheng, X. Yang, M. Sun, B. He, *Colloids Surf. A Physicochem. Eng. Asp.* 547 (2018) 28–36.

[24] T. Pasinszki, M. Krebsz, G.G. Lajgut, T. Kocsis, L. Kotai, S. Kauthale, S. Tekale, R. Pawar, *New J. Chem.* 42 (2018) 1092–1098.

[25] S. Schlichter, M. Rocha, A.F. Peixoto, J. Pires, C. Freire, M. Alvarez, *Polyhedron* 150 (2018) 69–76.

[26] J. Jiang, Y.S. Lim, S. Park, S.-H. Kim, S. Yoon, L. Piao, *Nanoscale* 9 (2017) 3873–3880.

[27] J. Jiang, G.H. Gunasekar, S. Park, S.-H. Kim, S. Yoon, L. Piao, *Mater. Res. Bull.* 100 (2018) 184–190.

[28] Y. Sun, L. Xu, Z. Yin, X. Song, J. Mater. Chem. A Mater. Energy Sustain. 1 (2013) 12361–12370.

[29] R. Cai, P.R. Ellis, J. Yin, J. Liu, C.M. Brown, R. Griffin, G. Chang, D. Yang, J. Ren, K. Cooke, P.T. Bishop, W. Theis, R.E. Palmer, *Small* 14 (2018) 1703734.

[30] B.M. Mogudi, P. Ncube, N. Bingwa, N. Mawila, S. Mathebula, R. Meijboom, *Appl. Catal. B* 218 (2017) 240–248.

[31] A. Ruban, B. Hammer, P. Stoltze, H.L. Skriver, J.K. Nørskov, *J. Mol. Catal. A Chem.* 115 (1997) 421–429.

[32] K. Karakas, A. Celebioglu, M. Celebi, T. Uyar, M. Zahmakiran, *Appl. Catal. B* 203 (2017) 549–562.

[33] R. Hu, T. Furukawa, Y. Gong, L. Chen, X. Wang, X. Tian, M. Nagatsu, *Adv. Mater. Interfaces* 5 (2018) 1800551.

[34] P. Ferrin, S. Kandoi, A.U. Nilekar, M. Mavrikakis, *Surf. Sci.* 606 (2012) 679–689.

[35] B. Hammer, J.K. Nørskov, *Advances in Catalysis*, Elsevier, 2000, pp. 71–129.

[36] A. Vojvodic, J.K. Nørskov, F. Abild-Pedersen, *Top. Catal.* 57 (2013) 25–32.

[37] E. Santos, W. Schmidkler, *ChemPhysChem* 7 (2006) 2282–2285.

[38] F. Calle-Vallejo, J.I. Martínez, J.M. García-Lastra, J. Rossmeisl, M.T. Koper, *Phys. Rev. Lett.* 108 (2012) 116103.

[39] Y. Sha, T.H. Yu, B.V. Merinov, W.A. Goddard, *ACS Catal.* 4 (2014) 1189–1197.

[40] I. Jimenez-Morales, S. Cavaliere, D. Jones, J. Roziere, *Phys. Chem. Chem. Phys.* 20 (2018) 8765–8772.

[41] F. Xu, Y. Le, B. Cheng, C. Jiang, *Appl. Surf. Sci.* 426 (2017) 333–341.

[42] S. Li, Y. Yang, L. Liu, Q. Zhao, *Chem. Eng. J.* 334 (2018) 1691–1698.

[43] T. Cai, L. Wang, Y. Liu, S. Zhang, W. Dong, H. Chen, X. Yi, J. Yuan, X. Xia, C. Liu, S. Lou, *Appl. Catal. B* 239 (2018) 545–554.

[44] J. Lao, R. Lv, J. Gao, A. Wang, J. Wu, J. Luo, *ACS Nano* 12 (2018) 12464–12471.

[45] H. Pan, X. Huang, R. Zhang, D. Wang, Y. Chen, X. Duan, G. Wen, *Chem. Eng. J.* 358 (2019) 1253–1261.

[46] D. Liu, R. Wang, W. Chang, L. Zhang, B. Peng, H. Li, S. Liu, M. Yan, C. Guo, J. Mater. Chem. A Mater. Energy Sustain. 6 (2018) 20887–20895.

[47] M. Alhabeb, K. Maleski, B. Anasori, P. Lelyukh, L. Clark, S. Sin, Y. Gogotsi, *Chem. Mater.* 29 (2017) 7633–7644.

[48] K. Li, T. Jiao, R. Xing, G. Zou, J. Zhou, L. Zhang, Q. Peng, *Sci. China Mater.* 61 (2018) 728–736.

[49] D. Magne, V. Mauchamp, S. Celierier, P. Chartier, T. Cabioch, *Phys. Chem. Chem. Phys.* 18 (2016) 30946–30953.

[50] L. Liu, R. Chen, W. Liu, J. Wu, D. Gao, J. Hazard. Mater. 320 (2016) 96–104.

[51] F. Xu, J. Zhang, B. Zhu, J. Yu, J. Xu, *Appl. Catal. B* 230 (2018) 194–202.

[52] X. Wu, Z. Wang, M. Yu, L. Xiu, J. Qiu, *Adv. Mater.* 29 (2017) 1607017.

[53] A. Lipatov, M. Alhabeb, M.R. Lukatskaya, A. Boson, Y. Gogotsi, A. Sinitskii, *Adv. Electron. Mater.* 2 (2016) 1600255.

[54] F. Xu, L. Zhang, B. Cheng, J. Yu, *ACS Sustainable Chem. Eng.* 6 (2018) 12291–12298.

[55] Y. Mei, Y. Lu, F. Polzer, M. Ballauff, M. Drechsler, *Chem. Mater.* 19 (2007) 1062–1069.

[56] F. Xu, W. Xiao, B. Cheng, J. Yu, *Int. J. Hydrogen Energy* 39 (2014) 15394–15402.

[57] J. Halim, K.M. Cook, M. Naguib, P. Eklund, Y. Gogotsi, J. Rosen, M.W. Barsoum, *Appl. Surf. Sci.* 362 (2016) 406–417.

[58] L. Liu, W. Liu, R. Chen, X. Li, X. Xie, *Chem. Eng. J.* 281 (2015) 804–812.

[59] F. Xu, B. Zhu, B. Cheng, J. Yu, J. Xu, *Adv. Opt. Mater.* 6 (2018) 1800911.

[60] Q. Zhao, L. Liu, R. Liu, L. Zhu, *Chem. Eng. J.* 353 (2018) 311–318.

[61] S. Li, L. Liu, Q. Zhao, C. He, W. Liu, *Phys. Chem. Chem. Phys.* 20 (2018) 3457–3464.

[62] Q. Zhao, L. Liu, S. Li, R. Liu, *Appl. Surf. Sci.* 465 (2019) 164–171.

[63] F. Xu, J. Zhang, B. Zhu, J. Yu, J. Xu, *Appl. Catal. B* 230 (2018) 194–202.

[64] W. Liu, R. Chen, L. Liu, S. Li, Z. Xue, C. He, *RSC Adv.* 6 (2016) 94451–94458.

[65] P. Zhao, X. Feng, D. Huang, G. Yang, D. Astruc, *Coord. Chem. Rev.* 287 (2015) 114–136.

[66] E. Blanco, P. Atienzar, P. Hernandez, C. Quintana, *Phys. Chem. Chem. Phys.* 19 (2017) 18913–18923.

[67] P. Chen, T. Zhou, M. Chen, Y. Tong, N. Zhang, X. Peng, W. Chu, X. Wu, C. Wu, Y. Xie, *ACS Catal.* 7 (2017) 7405–7411.